

# An Improved Non-local Planetary Boundary Layer Parameterization Scheme in Weather Forecasting and Research Model Based on a 1.5-order Turbulence Closure Model

W.L. Zhang<sup>1</sup>, J.C.H. Fung<sup>1,2</sup>, M.M.F. Wong<sup>1</sup>

<sup>1</sup>Division of Environment and Sustainability, Hong Kong University of Science and Technology, Hong Kong, China

<sup>2</sup>Department of Mathematics, Hong Kong University of Science and Technology, Hong Kong, China

## Key Points:

- The 1.5-order turbulence closure model has been incorporated in the ACM2 planetary boundary layer scheme in WRF
- High-resolution LiDAR observations are used to evaluate the performance of the new scheme over the summer and winter seasons in Hong Kong
- Vertical profiles of wind speeds are improved, with the most significantly improved metrics at the King's Park LiDAR site

## Abstract

Planetary boundary layer (PBL) modeling is a primary contributor to uncertainties in a numerical weather prediction model due to difficulties in modeling the turbulent transport of surface fluxes. The Weather Research and Forecasting model (WRF) has included many PBL schemes which may feature a non-local transport component driven by super-grid eddies or a one-and-half order turbulence closure model. In the present study, a turbulent kinetic energy (TKE)-based turbulence closure model is integrated into the non-local Asymmetric Convective Model version 2 (ACM2) PBL scheme and implemented in WRF. Non-local transport is modeled the same as ACM2 using the transilient matrix method. The new TKE-ACM2 PBL scheme is evaluated by comparing it with high spatiotemporal Doppler LiDAR observations in Hong Kong over 30 days each for summer and winter seasons to examine its capability in predicting the vertical structures of winds. Scatter plots of measured versus simulated instantaneous wind speeds show that TKE-ACM2 is able to reduce the root mean square error and mean bias and improve the index of agreement, especially at the urban observational site. The diurnal evolution of monthly averaged wind profiles suggests TKE-ACM2 can better match both the magnitudes and vertical gradients, revealing its superiority compared to ACM2 at stable atmospheric conditions. Other meteorological parameters including the potential temperature profiles, PBL heights, and surface wind speeds have also been investigated with references to various sources of observations.

## Plain Language Summary

Large uncertainties in a numerical weather prediction (NWP) model arise from difficulties in accurately modeling the planetary boundary layer (PBL) because of the chaotic turbulent motions of air. An adequate PBL parameterization scheme usually requires the consideration of turbulent transport due to large-scale buoyant plumes and a realistic while efficient turbulence closure model. The widely used NWP model, Weather Research and Forecasting (WRF) model, offers several PBL schemes, but few of them possess the aforementioned features simultaneously. Furthermore, little investigation has been done to examine the simulated vertical structures of wind speeds mainly constrained by the lack of high spatiotemporal resolution Doppler wind LiDAR data. In this research, we derived a new non-local PBL scheme that is based on the turbulent kinetic energy (TKE) turbulence closure model. Inter-scheme comparison as well as comparison against high spatiotemporal resolution observations have been carried out to examine the reliability of the new PBL scheme. It has been found that the new scheme outperforms others in reproducing the vertical profiles of wind speeds and PBL heights.

## 1 Introduction

Planetary boundary layer (PBL) is the lowest layer of the atmosphere in which the momentum and scalars are mixed more intensively than the free atmosphere driven by buoyancy effects and wind shear. The turbulent motions in the PBL are often subgrid-scale in a numerical weather prediction model (Shin & Hong, 2011), and their parameterizations are of paramount importance to correctly model a realistic atmospheric state (Holtlag & Steeneveld, 2009).

The Weather Research and Forecast model (WRF) (Skamarock et al., 2019) is one of the widely used mesoscale models to study regional weather patterns and offers several PBL schemes for users. The PBL schemes in WRF may feature a non-local transport component of surface fluxes, depending on whether the fluxes are allowed to be transported to non-adjacent cells. Development and evaluations of local closure schemes can be partially found in Bougeault and Lacarrere (1989); Janjić (1990, 1994); Sukoriansky et al. (2005); Bretherton and Park (2009), while those of non-local closure schemes can be referred to in Hong and Pan (1996); Pleim (2007a, 2007b); Hong et al. (2006). Al-

though the local closure schemes may model the transport of momentum and scalars relatively well under stable atmospheric conditions, their performance is barely satisfactory when strongly buoyant plumes arise when considerable positive surface heat fluxes are present (Holtslag & Boville, 1993). This can be attributed to the fact that uprising plumes whose size is comparable to the PBL depth can carry momentum and scalars at surface level up to about the top of PBL. To address the enhanced mixing by thermals, non-local closure schemes have introduced additional terms to model the upward transport due to buoyant plumes.

The Asymmetrical Convective Model version 2 (ACM2) (Pleim, 2007a, 2007b) is one of the non-local schemes that has utilized a transilient matrix to model the contribution of super-grid size eddies to turbulent transport. For a column of air, the turbulent transport at each model level is contributed to by local upward transport, non-local upward transport due to convectively buoyant plumes, and downward transport to compensate for subsidence. Under convective conditions, the transport of momentum and scalars will be enhanced at any cell above the first model layer but below the top of the PBL due to super-grid size eddies. Pleim (2007b) has shown that this non-local scheme can simulate vertical mixing reasonably well in mesoscale meteorological models and air quality models without sacrificing much efficiency using the sparse transilient matrix method. Xie et al. (2012, 2013) and Xie and Fung (2014) have also revealed that ACM2 outperforms many other schemes in terms of surface-level meteorological parameters such as wind speed at 10-m height ( $U_{10}$ ) and temperature at 2-m height ( $T_2$ ). However, ACM2 parameterizes the turbulence using a first-order closure model from Holtslag and Boville (1993) which prescribes the profiles of eddy viscosity,  $K_m$ , and eddy diffusivity,  $K_h$ , (hereinafter both referred to as  $K$ ) simply as a function of cubic height, neglecting the individual contributions of shear, buoyancy, and turbulent kinetic energy dissipation but instead consider their overall effects in a bulk way. The  $K$  profile has profound effects on all simulated meteorological quantities, and a more realistic representation of  $K$ , particularly one using a higher-order turbulence closure model, can greatly improve the three-dimensional meteorological field (e.g. X. Chen et al. (2022); Zonato et al. (2022)). Additionally, the first-order closure model of turbulence is unable to forecast the position and intensity of turbulence, leading to a poorly represented turbulent structure (Musson-Genon, 1995; Cuxart et al., 2006; Svensson & Holtslag, 2006).

This study focuses on improving the parameterization of  $K$  in ACM2 by replacing the bulk parameterization of turbulence with a higher-order, turbulent kinetic energy (TKE)-based model. In this work, the turbulence closure model derived from Bougeault and Lacarrere (1989) (hereinafter Boulac) is integrated into the original ACM2, which utilizes a prognostic equation to predict the spatiotemporal evolution of TKE. This approach reduces the extent of empiricism in calculating  $K$  and allows the turbulence intensity to be appreciated. To examine the performance of the proposed TKE-incorporated PBL scheme (TKE-ACM2), the instantaneous wind speeds and the diurnal evolution of monthly averaged wind profiles have been investigated and compared with observations for a 30-day simulation in summer and winter. The potential temperature profiles, PBL heights, and  $U_{10}$  are also evaluated using the sounding and surface observations.

## 2 Materials and Methods

### 2.1 Model formulation

The formulae presented in this section highlight the essence of the present PBL scheme (TKE-ACM2). A separate subroutine is prepared to package the TKE-ACM2 scheme in the simulation tool.

For a column of air to be mixed vertically, the governing prognostic equation for any Reynolds averaged prognostic meteorological variable  $\zeta$  reads,

$$\frac{\partial \zeta}{\partial t} = -\frac{\partial}{\partial z}(\overline{\zeta'w'}) = -\frac{\partial}{\partial z}(-K \frac{\partial \zeta}{\partial z}) \quad (1)$$

where  $\zeta$  can be zonal ( $u$ ) or meridional ( $v$ ) wind speed, potential temperature ( $\theta$ ), and water vapor mixing ratio ( $q$ );  $t$ ,  $z$  and  $w'$  represent time, height, and fluctuating vertical wind speed, respectively; the overbar represents the temporally averaged quantities (omitted for the prognostic quantity).

The representation of the non-local transport due to super-grid size eddies in the present work remains unchanged compared to the original ACM2. The detailed mathematical and physical formulation of ACM2 can be referred to in Pleim (2007b) and in its former version (Pleim & Chang, 1992). The discretized form of Equation 1 for  $i$ -th model layer ( $i > 1$ ) after adding the non-local transport terms reads,

$$\begin{aligned} \frac{\partial \zeta_i}{\partial t} = & f_{\text{conv}} \text{Mu} \zeta_1 - f_{\text{conv}} \text{Md}_i \zeta_i + f_{\text{conv}} \text{Md}_{i+1} \zeta_{i+1} \frac{\Delta z_{i+1}}{\Delta z_i} \\ & + (1 - f_{\text{conv}}) \frac{1}{\Delta z_i} \left[ \frac{K_{i+1/2} (\zeta_{i+1} - \zeta_i)}{\Delta z_{i+1/2}} - \frac{K_{i-1/2} (\zeta_i - \zeta_{i-1})}{\Delta z_{i-1/2}} \right] \end{aligned} \quad (2)$$

where subscript  $\pm 1/2$  denotes variables at the model face while integer subscript represents variables located at the center of the model layer,  $\Delta z$  is the vertical resolution,  $\text{Mu}$  represents the upward mixing rate [ $\text{s}^{-1}$ ],  $\text{Md}_i$  is the downward mixing rate from level  $i$  to its underlying layer [ $\text{s}^{-1}$ ],  $f_{\text{conv}}$  is a weighting factor that splits the total transport to local and non-local transport. According to Pleim (2007b), the mixing rates and weighting factor can be defined as

$$\text{Md}_i = \text{Mu} (h - z_{i-1/2}) / \Delta z_i \quad (3)$$

$$\text{Mu} = \frac{K_h (z_{1+1/2})}{\Delta z_{1+1/2} (h - z_{1+1/2})} \quad (4)$$

$$f_{\text{conv}} = \frac{K_h \gamma_h}{K_h \gamma_h - K_h \frac{\partial \theta}{\partial z}} \quad (5)$$

The correction term for  $\theta$  gradient,  $\gamma_h$ , is given by Holtslag and Boville (1993) and will be later used in the prognostic TKE equation. One should note this gradient adjustment term only applies in the convective PBL (CBL).

Note that the discretized governing equation of this work is identical to ACM2 (Pleim, 2007b), however, the key parameter,  $K$  which can be turbulent diffusivity or turbulent viscosity is computed by a one-and-half (1.5) order closure model. The PBL height (PBLH) is computed in the same way as in ACM2 which states the diagnostic PBLH ( $h$ ) in stable conditions can be expressed as:

$$h = \text{Ri}_{\text{crit}} \frac{\overline{\theta_v} U(h)^2}{g [\theta_v(h) - \theta_v(z_1)]} \quad (6)$$

where  $\theta_v$  is the virtual potential temperature,  $\overline{\theta_v}$  is the average virtual potential temperature between the first layer and the layer at which PBL caps,  $g$  the gravitational acceleration,  $z_1$  the height of the lowest model level, and  $\text{Ri}_{\text{crit}} = 0.25$  the critical Richardson number.

For unstable conditions, the PBLH in the new model stills follows the definition in Pleim (2007b) by finding the level at which the bulk Richardson number  $\text{Ri}_{\text{bulk}}$  first

exceeds  $Ri_{crit}$ .  $Ri_{bulk}$  is a dimensionless number that describes the dominance of averaged buoyancy over wind shear which is calculated using the wind speed difference at two layers corresponding to the layer at which the top of PBL is located and the unstable layer ( $z_{mix}$ ).  $Ri_{bulk}$  can be defined as follows as per Pleim (2007b):

$$Ri_{bulk} = \frac{g [\theta(h) - \theta_s] (h - z_{mix})}{\theta_v [U(h) - U(z_{mix})]^2} \quad (7)$$

where  $\theta_s$  is the gradient-adjusted virtual potential temperature by accounting for the non-local transport done by turbulent eddies of which size is comparable to PBLH (Holtslag et al., 1990).

The one-and-half order closure model is applied to compute  $K$  by retaining an extra prognostic equation for the second-order moment, TKE ( $e$ ). The basis for TKE prognostic equation is the energy cascade theory which describes that the chaotic motion of fluid particles results in the transfer of energy from larger to smaller scales (Richardson & Lynch, 2007). In the present work, the TKE prognostic equation follows that in Bougeault and Lacarrere (1989) which is a succeeding work of Therry and Lacarrère (1983):

$$\frac{\partial e}{\partial t} = -\frac{1}{\rho} \frac{\partial}{\partial z} \rho \overline{w'e} - \overline{u'w'} \frac{\partial u}{\partial z} - \overline{v'w'} \frac{\partial v}{\partial z} + \beta \overline{w'\theta'} - \epsilon \quad (8)$$

where the prime symbol in the superscript represents the fluctuating components,  $\rho$  is the density [ $\text{kg}/\text{m}^3$ ],  $\epsilon$  [ $\text{m}^2/\text{s}^3$ ] is the dissipation rate of TKE and is proportional to  $e^{3/2}$ ,  $\beta$  the buoyancy coefficient [ $\text{m}/\text{s}^2/\text{K}$ ]. One should note that for the turbulent transport of heat, the gradient adjustment term shall be applied in accordance with that in Equation 5 as follows:

$$\overline{w'\theta'} = \begin{cases} -K_h \left( \frac{\partial \theta}{\partial z} - \gamma_h \right) & , \text{ in the CBL} \\ -K_h \frac{\partial \theta}{\partial z} & , \text{ above the CBL} \end{cases} \quad (9)$$

Because an extra third-order moment (turbulent vertical transport of TKE) is introduced in Equation 8, additional parameterizations must be provided to close the equation. Similar to parameterizations of the second-order moments, the third-order moment can be related to an energy transfer coefficient ( $K_e$ ) and the vertical gradient of TKE:

$$\overline{w'e} = -K_e \frac{\partial e}{\partial z} \quad (10)$$

Eddy viscosity is related to TKE by empirical constants,

$$K_m = C_K l_k e^{1/2} \quad (11)$$

where  $C_K$  is the numerical coefficient ( $=0.4$  in Bougeault and Lacarrere (1989)), however, this proportionality constant may be varied to linearly scale  $K_m$  with  $e$ , e.g.,  $C_K = 0.55$  in X. Chen et al. (2022). Likewise, a value of  $0.6$  is used in the present study after performing several sensitivity tests.  $l_k$  is the characteristic length of eddies. Detailed determinations of empirical constants can be found in Bougeault and Lacarrere (1989). Eddy diffusivity and energy coefficient are subsequently related to eddy viscosity using the turbulent Prandtl numbers ( $Pr$ ). It should be noted that  $K_m$ ,  $K_h$ , and  $K_e$  are of the same magnitudes in both the present study and Bougeault and Lacarrere (1989) using  $Pr = 1$  whereas ACM2 uses  $Pr = 0.8$ .

The non-linear Equation 8 and Equation 10 are numerically solved by linearizing terms containing  $e$  and giving initial values of  $K$  and  $e$ . Subsequently, the explicit  $K$  can reduce the governing equation to a linear system of  $\mathbf{A}\bar{\zeta} = \bar{b}$  using the Crank-Nicolson scheme, where the square matrix  $\mathbf{A}$  is a bordered band diagonal matrix,  $\bar{\zeta}$  a column vector representing  $\zeta$  at all discretized levels, and  $\bar{b}$  the column vector containing explicit components. If we denote the element at  $i$ -th row and  $j$ -th column of  $\mathbf{A}$  as  $a_{i,j}$ , then the non-zero element of  $\mathbf{A}$  can be expressed as:

$$a_{i,i} = 1 + Cf_{\text{conv}} \text{Md}_i \Delta t + C(1 - f_{\text{conv}}) \frac{\Delta t}{\Delta z_i} (K_{i+1/2} \frac{1}{\Delta z_{i+1/2}} + K_{i-1/2} \frac{1}{\Delta z_{i-1/2}}) \quad (12)$$

$$a_{i,i+1} = -Cf_{\text{conv}} \text{Md}_i \frac{\Delta z_{i+1}}{\Delta z_i} \Delta t - C \frac{1}{\Delta z_i} K_{i+1/2} \frac{\Delta t}{\Delta z_{i+1/2}} \quad (13)$$

$$a_{i-1,i} = -C \frac{1}{\Delta z_i} K_{i-1/2} \frac{\Delta t}{\Delta z_{i-1/2}} \quad (14)$$

$$a_{i,1} = \begin{cases} -Cf_{\text{conv}} \text{Mu} \Delta t \\ 0 \end{cases}, \text{ above the CBL} \quad (15)$$

The element at  $i$ -th row of column vector  $\bar{b}$  is factorized to as,

$$b_i = \zeta_i^n + (1 - C)f_{\text{conv}} \text{Mu} \zeta_1^n \Delta t - (1 - C)f_{\text{conv}} \zeta_i^n \Delta t + (1 - C)f_{\text{conv}} \text{Md}_{i+1} \zeta_{i+1}^n \frac{\Delta z_{i+1}}{\Delta z_i} \Delta t + \frac{1 - C}{\Delta z_i} f_{\text{conv}} (K_{i+1/2} \frac{\zeta_{i+1}^n - \zeta_i^n}{\Delta z_{i+1/2}} - K_{i-1/2} \frac{\zeta_i^n - \zeta_{i-1}^n}{\Delta z_{i-1/2}}) \Delta t, \text{ in the CBL} \quad (16)$$

or,

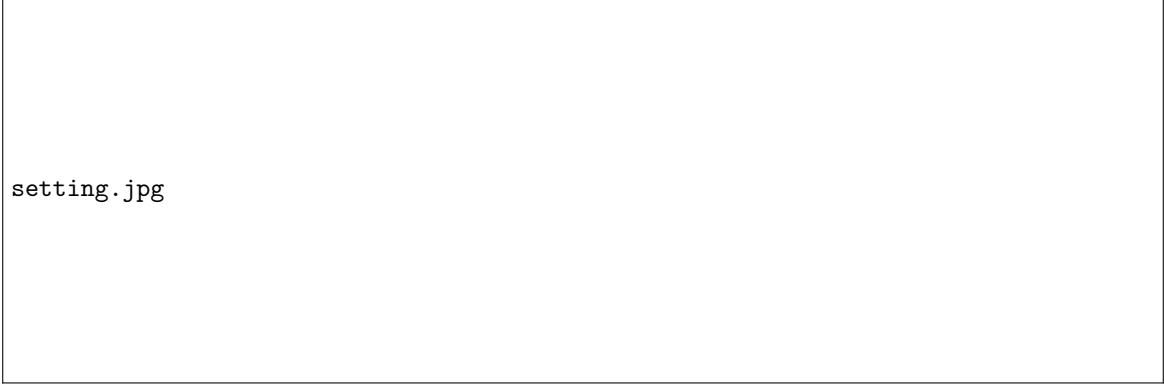
$$b_i = \zeta_i^n + \frac{1 - C}{\Delta z_i} f_{\text{conv}} (K_{i+1/2} \frac{\zeta_{i+1}^n - \zeta_i^n}{\Delta z_{i+1/2}} - K_{i-1/2} \frac{\zeta_i^n - \zeta_{i-1}^n}{\Delta z_{i-1/2}}) \Delta t, \text{ above the CBL} \quad (17)$$

where  $\Delta t$  is the discretized time step,  $C$  is the Crank-Nicolson number ( $=0.5$ ).

The turbulent surface fluxes are parameterized explicitly using the Monin-Obukhov similarity theory, which only acts on the first model layer in the absence of an urban model. Therefore, the explicitly parameterized surface fluxes will contribute to Equation 16 when  $i = 1$ . Consequently, the linear system  $\mathbf{A}\bar{\zeta} = \bar{b}$  is solved by lower-upper factorization with the back and forward substitution algorithm for any prognostic variable  $\zeta = \{u, v, \theta, q\}$ .

## 2.2 Model Configurations

WRF version 4.3 is used to simulate the atmospheric conditions for four nested domains (Figure 1a), with reference latitude and longitude of  $28.5^\circ\text{N}$  and  $114^\circ\text{E}$ , respectively, for the center of the largest Domain 1 (D1). D1 covers the whole of China including some other (parts of) East Asian countries. D2 includes southern and south-eastern China while D3 covers Guangdong province of China and several nearby provinces. D4 is the domain of interest that has the finest grid resolution and is characterized by highly urbanized and densely populated areas (Figure 1b). The locations of all sources of observations to evaluate the performance of the present study are highlighted in Figure 1b. The grid resolution ratio of each domain is 1:3 to its parent domain with a horizontal



setting.jpg

**Figure 1.** Domain configurations. (a) illustrates the four nested domains with a close-up of the finest domain in the right-bottom corner, and (b) shows urban cells in light blue, urban surface stations in red dots, non-urban surface stations in blue dots, the surface synoptic station for mixing heights observations in orange, and the three LiDAR units in purple within the finest domain (D4). Sounding measurements are carried out at the location adjacent to the KP LiDAR site.

resolution of D1 27 km, D2 9km, D3 3km, and D3 1km. The number of grid points (East-West  $\times$  North-South) are  $283 \times 184$ ,  $223 \times 163$ ,  $172 \times 130$ , and  $214 \times 163$  for D1 to D4.

39 eta levels are configured vertically up to 50-hPa pressure level corresponding to approximately 20km above ground level (AGL) to prevent numerical instability in the vertical direction, in particular, dense grids are created near the surface where the divergence of horizontal winds is large. The default 30-seconds 21-category Moderate Resolution Imaging Spectroradiometer (MODIS) land-use data is used to provide the land-cover classification for all domains. The National Centers for Environmental Prediction (NCEP) operational Global Forecast System (GFS) analysis data that is based on a 0.25 by 0.25-degree grid is used to provide the initial and boundary conditions for the simulated domains at a time interval of 6 hours.

The new TKE-ACM2 scheme is compared with two readily available PBL schemes in WRF: ACM2 and Boulac, since the new scheme shares common features and formulation with them. The aforementioned settings along with other key configurations are summarized in Table 1 which are the same when simulating using the three schemes. The simulation periods cover 30 days in the summer season from 15-Jun. (12 Universal Time Coordinated (UTC)). to 15 Jul. (12 UTC), and 30 days in the winter season from 30-Nov. (12 UTC) to 30-Dec. (12 UTC) in the year 2021. For each four-day simulation, the first day is used as a spin-up and is discarded in the analysis of results. The previous four-day segment will overlap one day with the later one. The simulated periods are chosen to be as little cloudy as possible to minimize bias caused by the microphysics scheme. The summer season in Hong Kong is characterized by the hottest period reaching  $\sim 30^\circ\text{C}$ , and the winter season stays as low as  $\sim 20^\circ\text{C}$  (Yan et al., 2021).

### 3 Results

#### 3.1 Instantaneous Wind Speed Profiles

There are many ways to analyze the simulated four-dimensional wind fields (three-dimensional in space and one-dimensional in time). We first present a comparison of in-

**Table 1.** Configurations of WRF version 4.3 settings for simulations using TKE-ACM2, ACM2, and Boulac PBL schemes

WRF version 4.3 Options	Settings
Meteorological data for boundary and initial conditions	NCEP GFS 0.25° by 0.25° latitudinal and longitudinal resolution with 6-hour interval
Grid resolutions	27km for D1 with 1:3 parent domain grid ratio for nested domains
Time steps	90s for D1 with 1:3 parent time step ratio for nested domains
Number of grid points (East-West × North-South)	D1 283 × 184, D2 223 × 163, D3 172 × 130, and D4 214 × 163
Number of vertical eta levels	39
Pressure at top model level	50hPa corresponding to approximately 20km AGL
Number of vertical levels in WRF Preprocessing System (WPS) output	34
Number of soil levels in WPS output	4
Microphysics scheme	WSM 3-class simple ice scheme (Hong et al., 2004)
Longwave radiation scheme	RRTMG scheme (Iacono et al., 2008)
Shortwave radiation scheme	RRTMG scheme (Iacono et al., 2008)
Surface layer scheme	Revised MM5 Monin-Obukhov scheme (Jiménez et al., 2012)
Land-surface scheme	Unified Noah land-surface model (F. Chen & Dudhia, 2001)
Cumulus scheme	Grell-Freitas ensemble scheme (Gall et al., 2013)
Urban model	Off for all domains; bulk surface flux parameterizations of which input is provided by the Noah land-surface model
Land-use data	21-class MODIS data
Grid nudging	6-hour interval grid analysis nudging only for D1
Observational nudging	Off for all domains

stantaneous wind speeds at multiple heights between the new TKE-AMC2 scheme and observations in Figure 2 for summer and in Figure 3 for winter. The observations are retrieved from the Doppler LiDAR units in Hong Kong averaged at 1-hr intervals and 25-m vertical increments. WRF simulation results are interpolated to the time steps and grids of observations. Note that in Figure 2 and Figure 3 which are scatterplots of all available measurements at several locations, we eliminate the dimensions of time and space, enabling the massive results over 30 days to be viewed as whole rather than presenting separate frames of instantaneous profiles. Thus, we are able to justify the pointwise agreement between observed and simulated instantaneous wind speeds along an air column over 30 days.



The Doppler LiDAR observational data measured at the Hong Kong University of Science and Technology Supersite (USTSS), Hok Tsui (HT), and King's Park (KP) are used to evaluate the performance of TKE-ACM2 (present study), ACM2, and Boulac PBL schemes. The tuning and setup of LiDAR units can be found in He et al. (2021). Each LiDAR is able to provide the zonal and meridional wind speed observations averaged at one hour up to  $\sim 3000\text{m}$ . The locations and corresponding land-use types of three LiDAR units can be found in Figure 1. USTSS is situated on the eastern shore of Clear Water Bay Peninsula of Hong Kong, facing Port Shelter and Sai Kung with few residential and commercial establishments in its surrounding land environment. The adjacent geography of USTSS also contains a bay area with few obstacles from sparse islands. HT is a rural area located in the southeast part of Hong Kong Island with even fewer obstacles in its surroundings. As opposed to the former two observational sites which are both rural areas, KP is characterized by much resistance of airflow due to lots of high and medium-rise buildings in its proximity. The land-use type at KP is much less permeable, leading to a totally different hydraulic property. The observational measurements made at the three sites have a relatively good representativity of Hong Kong (D4) meteorology considering they are able to represent the dominant land-use types. Data count for LiDAR observations at multiple heights at 25-m vertical increments and 1-hr intervals over 30 days at USTSS, HT, and KP are approximately 38,000, 35,000, and 35,000, respectively.

Several metrics are used to quantify the agreement between simulated results and observations at 1-hr intervals. Pearson's correlation coefficient (Corr.) measures the ratio of the covariance of observed and simulated wind speeds. Root mean square error (RMSE =  $1/N \sqrt{\sum_{i=1}^N (P_i - O_i)^2}$ ) demonstrates the square root of the second sample moment of the differences between predicted values and observed values, mean bias (MB =  $1/N \sum_{i=1}^N (P_i - O_i)$ ) measures the intrinsic differences, and index of agreement (IOA =  $1 - \frac{\sum_{i=1}^N |P_i - O_i|}{\sum_{i=1}^N (|P_i - \langle O_i \rangle| + |O_i - \langle O_i \rangle|)}$ ) indicates the overall agreement, where  $P_i$  and  $O_i$  are the predicted and observed values at  $i$ -th level over the simulation period,  $N$  the number of measurements at a certain time step,  $\langle \dots \rangle$  is the vertical ensemble average operator.

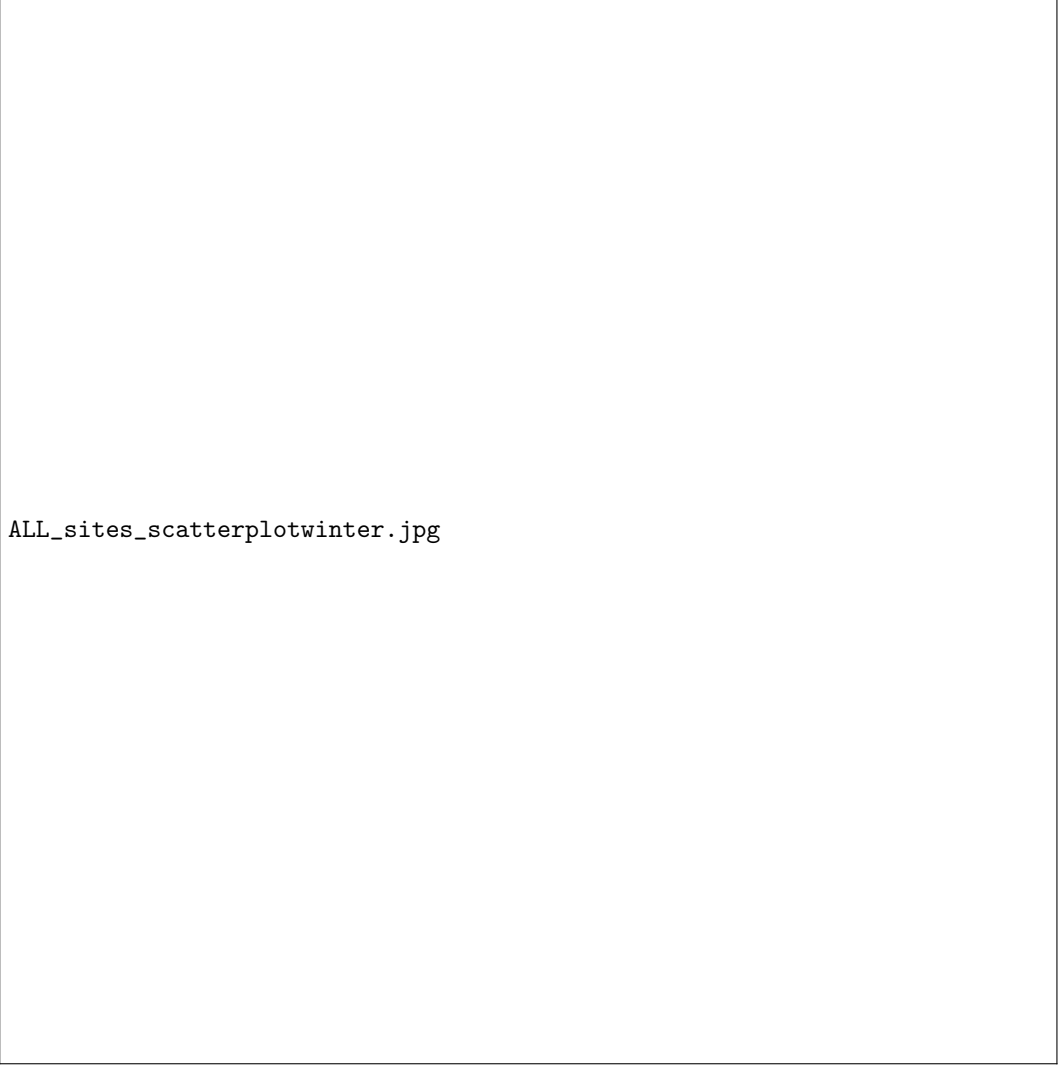
In the summer simulation case, it is found that TKE-ACM2 matches better with observations compared to the other two schemes, particularly the MB is reduced. The local scheme Boulac consistently yields underestimated wind speeds by up to 1m/s (at USTSS and HT) while the first-order scheme ACM2 generally overpredicts by up to 1.6m/s (at KP). As a comparison, MB of TKE-ACM2 is capped by positive 0.47m/s (at KP). Also, TKE-ACM2 has the least RMSE ( $\sim 2.2\text{m/s}$ ) at all sites compared to ACM2 having an RMSE up to 3.0m/s and Boulac reaching more than 2.4m/s, with the greatest advantages at KP. Thus, improved IOAs in TKE-ACM2 are consistently observed, exhibiting its strengthened abilities to reproduce more realistic wind speeds. The best alignment of TKE-ACM2 with observations is found for wind speeds near 4 and 8m/s (the area where dashed lines intersect the darkest regions in scatter plots).

In winter simulations, TKE-ACM2's performance is still robust, shown by the improved metrics. The general trend of all schemes' is to produce a positive bias in wind speeds in winter, with TKE-ACM2 and Boulac having a lower one compared to ACM2. Besides TKE-ACM2 producing smaller MB than ACM2, TKE-ACM2 also generates smaller RMSE compared to ACM2 and Boulac. Similar to the summer case, the greatest improvement of TKE-ACM2 is witnessed at KP which is located in a highly urbanized area. It is found that at this location, TKE-ACM2 has much better correlated wind speeds and the least biased wind magnitudes. Taking ACM2 as the base case, TKE-ACM2 improves Corr. and RMSE by 13.8% and 29.1%, reduces MB by 65.0%, and elevates IOA by 22.7% at KP. A possible explanation for TKE-ACM2 consistently yielding improved abilities in the urban area is that TKE-ACM2 relates both local and non-local transport



**Figure 2.** Instantaneous wind speeds at multiple heights comparison between simulations and observations in the summer season, with the third column results simulated using the new TKE-ACM2 scheme. Each sub-figure is labeled by the LiDAR site name followed by the scheme at the top left. The dashed line represents a slope of 1 between simulations and observations. Corr., RMSE, MB, and IOA are displayed at the bottom right of each sub-figure.

309 to TKE which is further corrected by superimposing the counter-gradient term on the  
 310 buoyancy production/ loss term in the TKE prognostic equation. In contrast, ACM2 com-  
 311 puts  $K$  using the local Richardson number which excludes the contribution of super-  
 312 grid eddies in the potential temperature gradient term, potentially leading to an inac-  
 313 curately reflected turbulence intensity. While Boulac ignores the large-scale gradients  
 314 of momentum and instead computes turbulent fluxes completely locally, its adequacy is  
 315 doubtful during convective conditions when turbulent eddy length scales surpass the ver-  
 316 tical grid increments (Pleim & Chang, 1992).



ALL\_sites\_scatterplotwinter.jpg

**Figure 3.** Same to Figure 2 but in the winter season.

### 3.2 Diurnal Evolution of Monthly Averaged Wind Profiles

Another angle to investigate the performance of TKE-ACM2 is to look at the diurnal evolution of monthly averaged wind profiles. Because many empirical parameters in a mesoscale numerical weather forecasting model are tuned based on averaged observational data over a certain timescale rather than attempting to fit instantaneous and scattered observed data points, a rational way to comprehend the performance of TKE-ACM is to analyze simulated results averaged for the whole month and for different hours. Figures 4, 5, and 6 plot the diurnal evolution of monthly averaged wind speeds where the upper half represents results in summer and the lower four sub-figures depict the results in winter, with error bars representing  $\pm 1$  standard deviation of monthly averaged measurements at  $i$ -th level. Note that the WRF simulated wind speeds have non-uniform vertical grids so they are linearly interpolated to the same grids of LiDAR measurements which start from 50m AGL and have an increment of 25m. Also, when LiDAR measurements encounter missing data at particular times and heights, the corresponding simulated wind speeds will be not taken into account for averaging.

AUSTSScombined\_vert.jpg

**Figure 4.** 30-day averaged vertical wind speed profile at USTSS observation site at each particular hour. Error bars in lighter colors indicate  $\pm 1$  standard deviation of measured wind speeds at the corresponding level.

AHTcombined\_vert.jpg

**Figure 5.** Same to 4 but at HT LiDAR location.

AKPcombined\_vert.jpg

**Figure 6.** Same to 4 but at KP LiDAR location.

Figure 4 suggests that at USTSS, TKE-ACM2 shows improved alignments during summer by having reduced MB and greater IOA compared to ACM2 and Boulac. In general, ACM2 consistently overpredicts the wind speeds while Boulac yields underestimated results. A closer inspection shows that on average ACM2 overpredicts the wind speeds by 0.70m/s, Boulac underestimates by 1.14m/s, and TKE-ACM2 has the least MB with -0.04m/s. RMSE indicates that TKE-ACM2 spreads the least against observations (RMSE=0.76m/s) compared to ACM2 (1.34m/s) and Boulac (1.46m/s) during summer. TKE-ACM2 has an average IOA of 0.87 while the other two stay below 0.80. Additionally, TKE-ACM2 consistently shows the highest correlation coefficients. In the winter simulations, TKE-ACM2 virtually collapses to Boulac with only slight differences from 300m to 800m where TKE-ACM2 is marginally closer to observations, and the two schemes show greater agreements with observations with both average IOAs reaching 0.88 compared to ACM2 which has an average IOA of 0.71. Also, the RMSE and MB produced by TKE-ACM2 and Boulac are more satisfactory during winter, especially at nighttime. The reason for the first-order scheme ACM2 to deviate the most during nighttime can largely be attributed to the inability to model the turbulence mixing under stable conditions due to the absence of convective plumes. During the daytime, ACM2 can have a closer match possibly caused by the compensation of non-local transport.

Vertical structures at another rural LiDAR site HT reveal that during summer TKE-ACM2 exhibits best agreements during the daytime, while the local scheme Boulac is found to better align with observations from 18LT to 23LT. Similar to the trends found at USTSS, ACM2 consistently overestimates wind speeds at most heights at HT (MB=0.80m/s), with Boulac often underestimating by -1.01m/s and TKE-ACM2 having the least bias (0.26m/s) during summer. IOAs for the summer case show that TKE-ACM2 on average scores a value of 0.77, which outperforms ACM2 of 0.65 and Boulac of 0.69. It is found that three schemes will collapse to a similar profile from 13LT to 20LT in winter at this rural LiDAR station, which is also observed at USTSS. It implies that during gently to moderately convective conditions, the contributions of large-scale eddies to turbulent mixing have minimum impacts on the vertical wind profiles. While transiting to nighttime stable conditions, the first-order model ACM2 deviates more than the TKE-based models by having a large positive bias from the surface height to  $\sim 800$ m. A conclusion drawn from the winter simulations at HT is that Boulac and TKE-ACM2 predict almost the same profiles across a diurnal cycle, with the first-order ACM2 scheme likely yielding positive bias during stable conditions. This finding shows consistency for both USTSS and HT rural sites.

Results in summer at the urban LiDAR site KP show different patterns compared to those at USTSS and HT. From 08LT to 17LT, TKE-ACM2 generally predicts the wind speeds with the least bias and matches the best, especially for altitudes from  $\sim 300$  to 800m. At the same time, its performance for heights below 300m shows slight overpredictions. However, it should be noted that the urban model is not incorporated in this study so the urban morphology is completely missing. Since the KP LiDAR site and its proximity is surrounded by many buildings whose heights are mostly above 100m, the interpretations of wind speeds near the surface should be paid with extra attention. From 17LT to 24LT, Boulac outperforms TKE-ACM2, while ACM2 has a positive bias of up to 4.0m/s at  $\sim 375$ m. From 02LT to 07LT, TKE-ACM2 reproduces wind profiles of minimum bias at each level. Statistically, in the summer simulations, TKE-ACM2 and Boulac have average IOAs of 0.85, but TKE-ACM2 has slightly lower RMSE and MB. In general, ACM2's performance is the least satisfactory with an average IOA of 0.52, RMSE of 1.94m/s, and MB of 1.46m/s in summer. When the heat forcing is reduced in winter at KP, TKE-ACM2 has consistent superiorities compared to ACM2 and Boulac. Large inter-scheme differences are found below  $\sim 800$ m where ACM2 deviates the most by yielding a large positive bias and Boulac overpredicts by up to 3.0m/s. Above a certain height of about 800m, three schemes collapse to a similar profile. The statistics have revealed that at KP in winter, TKE-ACM2 greatly elevates IOA from 0.45 (ACM2) and 0.68 (Boulac)

to 0.86. Besides, TKE-ACM2 has the smallest RMSE of 1.06m/s and MB of 0.81m/s, which account for 60.1% improvements in RMSE and 59.5% in MB compared to ACM2. Lastly, TKE-ACM2 can better match the wind shears, reflected by the greatest Pearson's correlation coefficient of 0.93.

Conclusively, the monthly averaged wind profiles suggest that TKE-ACM2 and Boulac show consistent advantages at rural sites at nighttime compared to the first-order ACM2 scheme, with Boulac showing even better performance from 18LT to 23LT at rural sites in summer. However at convective hours during summer, TKE-ACM2 can better match observations at rural sites. Three schemes may reproduce very similar wind profiles in winter, but ACM2 is positively biased for heights below  $\sim 800$ m. At the urban LiDAR site, TKE-ACM2 exhibits good alignments with observations, especially in winter where the other two schemes display positive bias. The aforementioned discoveries imply that the non-local transport components in TKE-ACM2 are particularly beneficial compared to Boulac at convective hours when surface heat flux is significant. Also, the introduction of a TKE-based  $K$  is superior to ACM2 under stable atmospheric conditions.

Box plots of metrics for the diurnal evolution of averaged wind profiles which correspond to each sub-plot in Figures 4, 5, and 6 are drawn in Figure 7. Each sub-figure in Figure 7 shows the distribution of the metrics where Figure7a indicates summer and Figure7b is for winter, accounting for {RMSE, MB, ME, NME, IOA, Corr.}.



**Figure 7.** Distribution of metrics of vertical wind speed profiles averaged at 24 hours in (a) summer and (b) winter. White dots indicate the mean values.

Figure 7 indicates that in most cases TKE-ACM2 has the lowest mean RMSE, MB, ME, and NME. Significant improvements in IOA are observed at USTSS and HT in summer and at KP in winter. In general, TKE-ACM2 and Boulac have the best correlated wind profiles.



### 3.3 Vertical Potential Temperature Profiles Averaged at 08 and 20 Local Time

This section presents the simulated and observed potential temperature profiles to partially examine the performance of schemes in passive scalar transport. The upper-air measurements of temperature are taken by the Automatic Upper-air Sounding System at King's Park meteorological station which is very close to where KP LiDAR is deployed. The measured temperature at certain pressure levels from sounding instruments deployed at KP is converted to potential temperature (Equation 18) and plotted against WRF simulations in Figure 8 for summer (upper panel) and winter cases (lower panel), respectively. Due to the constraint that sounding balloons equipped with radiosondes are launched only at certain synoptic hours, we are only able to present the comparison of potential temperature profiles at 08 LT and 20 LT.

$$\theta = T \left( \frac{P_0}{P} \right)^{R/c_p} \quad (18)$$

where  $T$  is the measured temperature;  $P_0$  the reference pressure;  $P$  the corresponding pressure at which  $T$  is measured;  $R = 287\text{J/K/kg}$  and  $c_p = 1004\text{J/K/kg}$ .

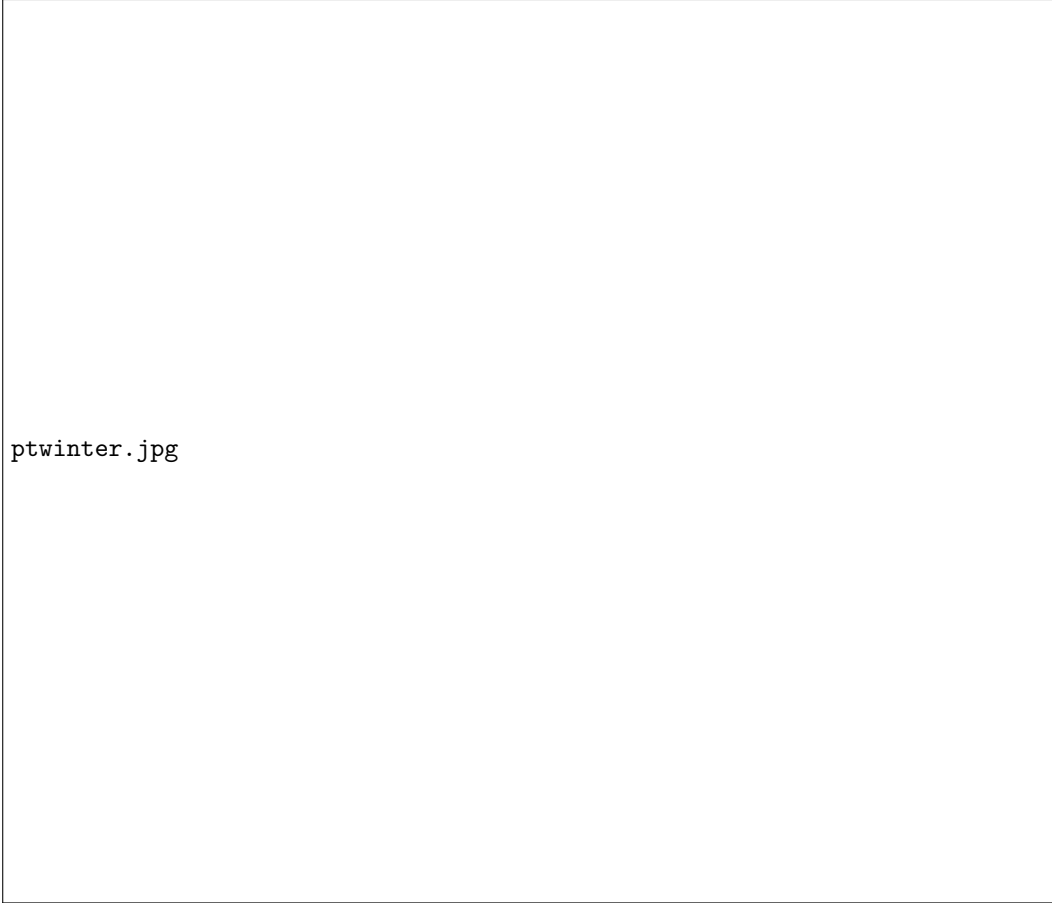


**Figure 8.** Potential temperature profile averaged at 08 LT and 20 LT at KP sounding station. The upper panel demonstrates the comparison in the summer season while the lower panel indicates the winter season. Shared regions and horizontal bars depict the variabilities for 30 days.

All schemes are able to reproduce a similar pattern of averaged potential temperature profiles, particularly in winter where the magnitudes differ by little. During summer, all schemes tend to yield a cold bias by up to  $-1.25$  °C (Boulac at 975 hPa at 08LT). The new TKE-ACM2 scheme seems to produce potential temperatures of which magnitudes situate between those generated by Boulac and ACM2. The differences between ACM2 and TKE-ACM2 are mainly attributable to the turbulence closure models and the eddy Prandtl numbers ( $Pr$ ). It is shown that  $Pr$  is negatively correlated to temperature during the daytime (C. Zhang et al., 2022) so it may explain an enlarged cold bias in TKE-ACM2 where a larger  $Pr = 1$  is used compared to that  $Pr = 0.8$  in ACM2. Despite the parameterization schemes can reproduce potential temperature profiles of similar patterns, the vertical spatial resolution and time resolution of observations are insufficient to examine detailed vertical transport of passive scalar. Also, considering the drifting of rising balloons, the measured temperature may only have good indications at lower levels. Thus, it is recommended to obtain high-quality vertical structures of the passive scalar prior to studying passive scalar transport, such as the dispersion modeling of air pollutants.

### 3.4 Planetary Boundary Layer Heights

Surface synoptic observations of mixing heights at a 3-hr interval during daytime at  $22.32^{\circ}\text{N}$ ,  $114.17^{\circ}\text{E}$  (marked as the orange square in Figure 1b) are used to validate the planetary boundary layer heights (PBLH) calculated from the new TKE-ACM2 scheme. The averaged values of mixing heights/ PBLH for each simulation period are plotted in Figure 9.

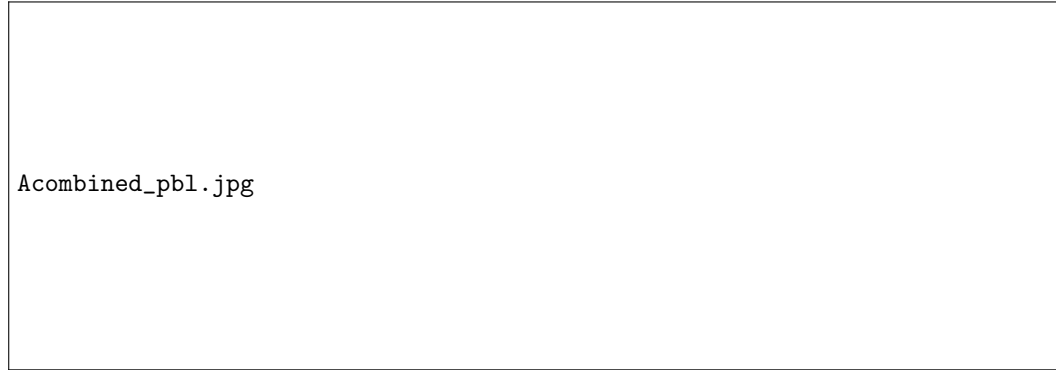


**Figure 9.** Averaged mixing heights/ PBLH during daytime. Shaded regions and vertical lines depict the variabilities of PBLH/ mixing heights.

During the summer season, TKE-ACM2 reports the lowest peak PBLH reaching  $\sim 1000\text{m}$  at 14LT, which is the closest to observed mixing heights (987m). At 11LT and 17LT when the solar radiation is less intensive, TKE-ACM2 also simulates the shortest while the most accurate PBLH among all schemes. ACM2 and Boulac tend to yield a PBLH that is consistently higher than observed mixing heights, with ACM2 generating a greater positive bias PBLH from 10LT to 17LT. In the winter season, all schemes collapse into a similar PBLH that is on average  $\sim 150\text{m}$  shorter than that in summer and none of them deviates significantly from observations.

It should be reminded that the PBLH is calculated in an identical way in ACM2 and TKE-ACM2 by finding the layer of which  $Ri$  first exceeds the critical value of  $Ri_{\text{crit}} = 0.25$ , while Boulac prescribes the height at which TKE reduces to a critical value to be the top of PBL. The differences between ACM2 and TKE-ACM2 may be mainly driven

by the differences in wind profiles since Figure 8 indicates that the potential temperature does not differ much in either season.

### 3.5 Surface Wind Speeds Over 33 Stations

Apart from the vertical profiles of wind speeds, another remaining question is to what extent the surface wind speeds simulated by TKE-ACM2 match observations. We plotted the time series of  $U_{10}$  at 33 stations in D4 consisting of 17 urban stations and 16 non-urban stations (marked as red and black in Figure 1) in Figure 10 for summer and in Figure 11 for winter, with rainy days excluded. Table 2 summarizes the performance of TKE-ACM2 compared to ACM2 and Boulac.

**Table 2.** Summary of metrics for  $U_{10}$  at urban and non-urban surface stations. Numbers in bold represent the best ones out of the three schemes.

	Urban			Non-urban		
	ACM2	Boulac	TKE-ACM2	ACM2	Boulac	TKE-ACM2
<i>Summer</i>						
RMSE	2.39	<b>0.99</b>	1.47	1.29	<b>0.94</b>	1.59
MB	1.99	<b>-0.14</b>	0.97	1.15	<b>0.52</b>	1.41
IOA	0.43	<b>0.56</b>	0.53	0.74	<b>0.79</b>	0.71
<i>Winter</i>						
RMSE	1.80	1.47	<b>1.26</b>	1.88	1.60	<b>1.53</b>
MB	1.76	1.19	<b>1.18</b>	1.60	<b>1.00</b>	1.20
IOA	0.44	0.42	<b>0.49</b>	0.63	0.65	<b>0.70</b>

It is found that TKE-ACM2 does not produce  $U_{10}$  as accurately as Boulac in either urban or non-urban areas during summer, although it produces a positive MB of almost halved that of ACM2 in urban areas. In winter, TKE-ACM2 performs slightly better than ACM2 and Boulac albeit the positive bias still persists. Nonetheless,  $U_{10}$  only represents the flow property at a single height (10m) which can be sensitive to the model setup, such as the surface layer scheme ((Srinivas et al., 2016)). Thus, we plan to investigate the optimal combinations of different parameterizations with the new TKE-ACM2 PBL scheme that could better reproduce  $U_{10}$ . In this study, the main focus lies on the vertical structures of wind speeds which are validated using LiDAR observations below 1500m. It should be also noted that the urban model is not used in this study due to the incompatibility of ACM2 with the urban model (Dy et al., 2019; Bhautmage et al., 2022). Thus, the overestimations in  $U_{10}$  by ACM2 and TKE-ACM2 can be explained by the lack of additional momentum drag caused by the densely built environment in our domain 4. Motivated by these concerns, we propose to incorporate the multi-layer urban model in WRF, Building Effect Parameterization (BEP, (Martilli et al., 2002)), into the new TKE-ACM2 scheme in future work. To accomplish that, we aim to superimpose the implicit components from BEP on the square matrix  $\mathbf{A}$  and the explicit components on the column vector  $\bar{b}$  to represent the multi-layer urban effects on the prognostic variables  $\zeta$  and  $e$ .

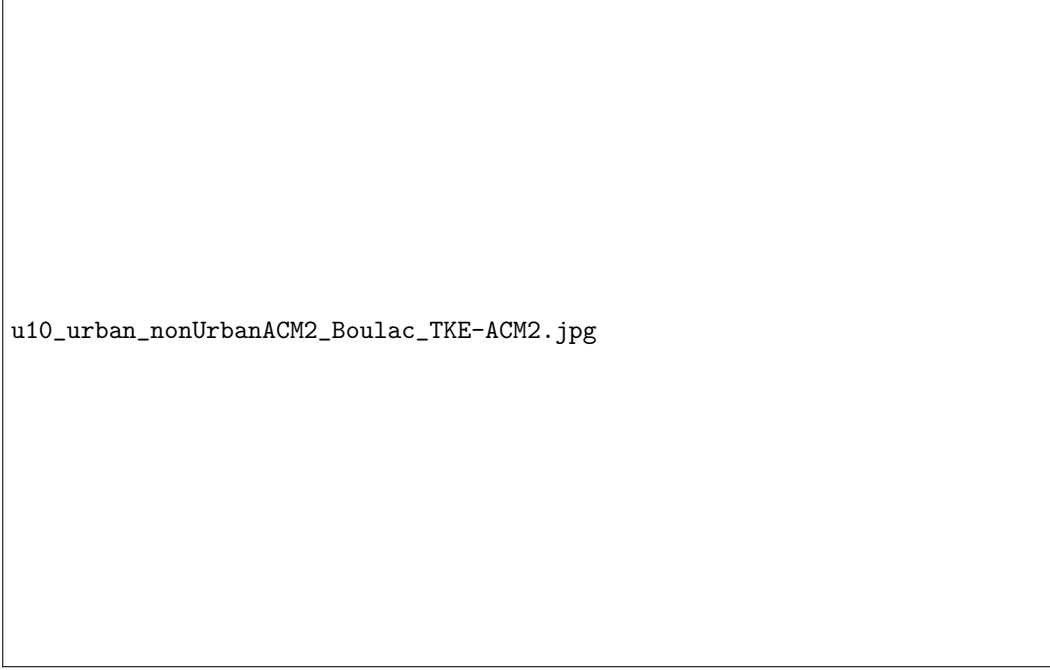


**Figure 10.** Averaged  $U_{10}$  time series in summer. The top panel indicates the averaged  $U_{10}$  for 17 urban sites and the bottom panel indicates the 16 non-urban stations. Shaded regions in grey color indicate the variabilities of measured  $U_{10}$  across stations. Rainy days are excluded.

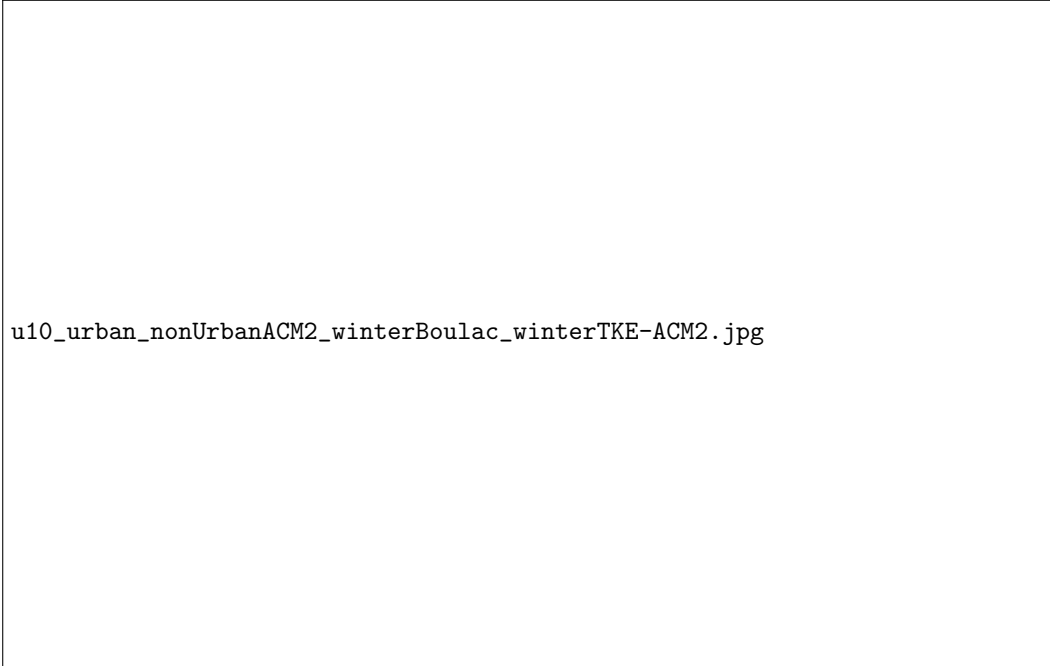


**Figure 11.** Same to Figure 10 but in winter.

## 4 Conclusions

A new planetary boundary layer scheme using the same non-local transport framework in ACM2 but a different sub-grid turbulence model is developed and implemented in WRF. The new TKE-ACM2 scheme has utilized a similar TKE-based turbulence closure model in Boulac and has been tested for two 30-day simulations in summer and winter in the Hong Kong region. The 1-hr interval with 25-m increment Doppler LiDAR observations deployed in USTSS, HT, and KP in Hong Kong are used as the ground truth to evaluate the performance of TKE-ACM2. Also, the sounding data measuring the potential temperature at KP at 08 and 20 local times is used to examine the ability of TKE-ACM2 in passive scalar transport. Mixing heights measured at the 3-hr frequency during the daytime are utilized to verify the reliability of the planetary boundary layer heights generated by TKE-ACM2. Lastly, the 10-m wind observations have implied that potential improvements can be carried out in TKE-ACM2 by accounting for the necessary momentum drag in urban areas.

Scatterplots of instantaneous wind speeds for more than a total of 118,000 measurement points in each season at three locations suggest that TKE-ACM2 has successfully reduced RMSE and MB and improved IOA compared to the other two schemes in WRF, ACM2, and Boulac. The enhanced capability in predicting instantaneous wind speeds is consistent for simulations in two seasons. In particular, the most notable improvements are observed at KP which is characterized by a highly urbanized area, with improvements of 29.1% in RMSE, 65.0% in MB, and 22.7% in IOA compared to ACM2 in winter.

The comparison of the diurnal evolution of monthly averaged wind profiles indicates that TKE-ACM2 in general aligns best among selected schemes. The six chosen metrics show consistent improvements by TKE-ACM2 in both summer and winter simulations. It can be concluded that TKE-ACM2 outperforms Boulac during convective hours while significant advantages are found at stable atmospheric conditions compared to ACM2 at rural LiDAR sites. This has shown the necessity of including the non-local transport by large-scale eddies at convective hours and the superiority of the TKE-based turbulence closure methods which are simultaneously integrated in TKE-ACM2. TKE-ACM2 reproduces the most accurate results at the urban LiDAR site, particularly during winter where the mean IOA is elevated from 0.45 (ACM2) and 0.68 (Boulac) to 0.86.

Mixing heights observations indicate that TKE-ACM2 predicts the shortest while the most reliable PBLH during the daytime in summer, with ACM2 and Boulac consistently generating positive bias by up to 150m at 14LT. The PBLH simulated by the three schemes exhibit great similarities and show good agreement during winter.

$U_{10}$  time series have revealed that TKE-ACM2 may predict overestimated results during summer, despite it has shown improvements compared to ACM2. During winter, TKE-ACM2 produces satisfactory results but still with positive bias persisting. It implies that TKE-ACM2 may further be improved by coupling with the urban model, BEP, in WRF to account for the additional momentum drag at near-surface levels caused by the highly built environment in the selected domain. It is anticipated that  $U_{10}$  can be lowered in urban areas by introducing the multi-layer urban model.

## 5 Open Research

The WRF model version 4.3 can be downloaded from <https://www.mmm.ucar.edu/> [Software]. The initial and boundary conditions for the WRF model can be obtained through NCEP via <https://rda.ucar.edu/datasets/> [Dataset]. Doppler LiDAR observations, sounding data, and surface station observations can be obtained from [https://envf.ust.hk/dataview/mm\\_plot/current/](https://envf.ust.hk/dataview/mm_plot/current/) upon request to the corresponding author [Dataset]. The WRF model that contains TKE-ACM2 used in this study can be found in W. Zhang et al. (2023) [Software].

## Acknowledgments

We appreciate the assistance of the Hong Kong Observatory (HKO), which provided the meteorological data. The work described in this paper was supported by a grant from the Research Grants Council of the Hong Kong Special Administrative Region, China (Project Nos. C6026-22G).

## References

- Bhautmage, U. P., Fung, J. C. H., Pleim, J., & Wong, M. M. F. (2022). Development and Evaluation of a New Urban Parameterization in the Weather Research and Forecasting (WRF) Model. *Journal of Geophysical Research: Atmospheres*, 127(16). doi: 10.1029/2021JD036338
- Bougeault, P., & Lacarrere, P. (1989). Parameterization of Orography-Induced Turbulence in a Mesobeta-Scale Model. *Monthly Weather Review*, 117(8), 1872 – 1890. doi: 10.1175/1520-0493(1989)117(1872:POOITI)2.0.CO;2
- Bretherton, C. S., & Park, S. (2009). A New Moist Turbulence Parameterization in the Community Atmosphere Model. *Journal of Climate*, 22(12), 3422–3448. doi: 10.1175/2008JCLI2556.1
- Chen, F., & Dudhia, J. (2001). Coupling an Advanced Land Surface–Hydrology Model with the Penn State–NCAR MM5 Modeling System. Part I: Model Implementation and Sensitivity. *Monthly Weather Review*, 129(4), 569 – 585. doi: [https://doi.org/10.1175/1520-0493\(2001\)129\(0569:CAALSH\)2.0.CO;2](https://doi.org/10.1175/1520-0493(2001)129(0569:CAALSH)2.0.CO;2)
- Chen, X., Bryan, G. H., Hazelton, A., Marks, F. D., & Fitzpatrick, P. (2022). Evaluation and Improvement of a TKE-Based Eddy-Diffusivity Mass-Flux (EDMF) Planetary Boundary Layer Scheme in Hurricane Conditions. *Weather and Forecasting*, 37(6), 935–951. doi: 10.1175/WAF-D-21-0168.1
- Cuxart, J., Holtslag, A. A. M., Beare, R. J., Bazile, E., Beljaars, A., Cheng, A., ... Xu, K.-M. (2006, February). Single-Column Model Intercomparison for a Stably Stratified Atmospheric Boundary Layer. *Boundary-Layer Meteorology*, 118(2), 273–303. Retrieved from <https://doi.org/10.1007/s10546-005-3780-1> doi: 10.1007/s10546-005-3780-1
- Dy, C. Y., Fung, J. C. H., & Pleim, J. (2019). Momentum Drag Effect Over Urbanized Areas in the ACM2 PBL Component of the WRF model. *Journal of Geophysical Research: Atmospheres*, 124(8), 4460–4476. doi: 10.1029/2018JD029333
- Gall, R., Franklin, J., Marks, F., Rappaport, E. N., & Toepfer, F. (2013). The Hurricane Forecast Improvement Project. *Bulletin of the American Meteorological Society*, 94(3), 329 – 343. doi: <https://doi.org/10.1175/BAMS-D-12-00071.1>
- He, Y., Ren, C., Mak, H. W. L., Lin, C., Wang, Z., Fung, J. C. H., ... Ng, E. (2021). Investigations of high-density urban boundary layer under summer prevailing wind conditions with Doppler LiDAR: A case study in Hong Kong. *Urban Climate*, 38, 100884. doi: <https://doi.org/10.1016/j.uclim.2021.100884>
- Holtslag, A. A. M., & Boville, B. A. (1993). Local Versus Nonlocal Boundary-Layer Diffusion in a Global Climate Model. *Journal of Climate*, 6(10), 1825 – 1842. doi: 10.1175/1520-0442(1993)006<1825:LVNBLD>2.0.CO;2
- Holtslag, A. A. M., Bruijn, E. I. F. D., & Pan, H.-L. (1990). A High Resolution Air Mass Transformation Model for Short-Range Weather Forecasting. *Monthly Weather Review*, 118(8), 1561 – 1575. doi: 10.1175/1520-0493(1990)118(1561:AHRAMT)2.0.CO;2
- Holtslag, A. A. M., & Steeneveld, G.-J. (2009). Single Column Modeling of Atmospheric Boundary Layers and the Complex Interactions with the Land Surface. In R. A. Meyers (Ed.), *Encyclopedia of Complexity and Systems Science* (pp. 8139–8153). New York, NY: Springer New York. doi: 10.1007/978-0-387-30440-3\_482
- Hong, S.-Y., Dudhia, J., & Chen, S.-H. (2004). A Revised Approach to Ice Micro-

- physical Processes for the Bulk Parameterization of Clouds and Precipitation. *Monthly Weather Review*, 132(1), 103 – 120. doi: [https://doi.org/10.1175/1520-0493\(2004\)132\(0103:ARATIM\)2.0.CO;2](https://doi.org/10.1175/1520-0493(2004)132(0103:ARATIM)2.0.CO;2)
- Hong, S.-Y., Noh, Y., & Dudhia, J. (2006). A New Vertical Diffusion Package with an Explicit Treatment of Entrainment Processes. *Monthly Weather Review*, 134(9), 2318–2341. doi: 10.1175/MWR3199.1
- Hong, S.-Y., & Pan, H.-L. (1996). Nonlocal Boundary Layer Vertical Diffusion in a Medium-Range Forecast Model. *Monthly Weather Review*, 124(10), 2322 – 2339. doi: [https://doi.org/10.1175/1520-0493\(1996\)124\(2322:NBLVDI\)2.0.CO;2](https://doi.org/10.1175/1520-0493(1996)124(2322:NBLVDI)2.0.CO;2)
- Iacono, M. J., Delamere, J. S., Mlawer, E. J., Shephard, M. W., Clough, S. A., & Collins, W. D. (2008). Radiative forcing by long-lived greenhouse gases: Calculations with the AER radiative transfer models. *Journal of Geophysical Research: Atmospheres*, 113(D13). doi: <https://doi.org/10.1029/2008JD009944>
- Janjić, Z. I. (1990). The Step-Mountain Coordinate: Physical Package. *Monthly Weather Review*, 118(7), 1429–1443. doi: 10.1175/1520-0493(1990)118(1429:TSMCPP)2.0.CO;2
- Janjić, Z. I. (1994). The Step-Mountain Eta Coordinate Model: Further Developments of the Convection, Viscous Sublayer, and Turbulence Closure Schemes. *Monthly Weather Review*, 122(5), 927–945.
- Jiménez, P. A., Dudhia, J., González-Rouco, J. F., Navarro, J., Montávez, J. P., & García-Bustamante, E. (2012). A Revised Scheme for the WRF Surface Layer Formulation. *Monthly Weather Review*, 140(3), 898 – 918. doi: <https://doi.org/10.1175/MWR-D-11-00056.1>
- Martilli, A., Clappier, A., & Rotach, M. W. (2002). An Urban Surface Exchange Parameterisation for Mesoscale Models. *Boundary-Layer Meteorology*, 104(2), 261–304. doi: 10.1023/A:1016099921195
- Musson-Genon, L. (1995). Comparison of different simple turbulence closures with a one-dimensional boundary layer model. *Monthly weather review*, 123(1), 163–180. (ISBN: 1520-0493)
- Pleim, J. E. (2007a). A Combined Local and Nonlocal Closure Model for the Atmospheric Boundary Layer. Part II: Application and Evaluation in a Mesoscale Meteorological Model. *Journal of Applied Meteorology and Climatology*, 46(9), 1396–1409. doi: 10.1175/JAM2534.1
- Pleim, J. E. (2007b). A Combined Local and Nonlocal Closure Model for the Atmospheric Boundary Layer. Part I: Model Description and Testing. *Journal of Applied Meteorology and Climatology*, 46(9), 1383–1395. doi: 10.1175/JAM2539.1
- Pleim, J. E., & Chang, J. S. (1992). A non-local closure model for vertical mixing in the convective boundary layer. *Atmospheric Environment. Part A. General Topics*, 26(6), 965–981. doi: [https://doi.org/10.1016/0960-1686\(92\)90028-J](https://doi.org/10.1016/0960-1686(92)90028-J)
- Richardson, L. F., & Lynch, P. (2007). *Weather Prediction by Numerical Process* (2nd ed.). Cambridge: Cambridge University Press. doi: 10.1017/CBO9780511618291
- Shin, H. H., & Hong, S.-Y. (2011, May). Intercomparison of Planetary Boundary-Layer Parametrizations in the WRF Model for a Single Day from CASES-99. *Boundary-Layer Meteorology*, 139(2), 261–281. doi: 10.1007/s10546-010-9583-z
- Skamarock, W. C., Klemp, J. B., Dudhia, J., Gill, D. O., Liu, Z., Berner, J., ... Barker, D. M. (2019). A description of the advanced research WRF model version 4. *National Center for Atmospheric Research: Boulder, CO, USA*, 145(145), 550.
- Srinivas, C. V., Hari Prasad, K. B. R. R., Naidu, C. V., Baskaran, R., & Venktraman, B. (2016, February). Sensitivity Analysis of Atmospheric Dispersion Simulations by FLEXPART to the WRF-Simulated Meteorological Predic-



- tions in a Coastal Environment. *Pure and Applied Geophysics*, 173(2), 675–700. Retrieved from <https://doi.org/10.1007/s00024-015-1104-z> doi: 10.1007/s00024-015-1104-z
- Sukoriansky, S., Galperin, B., & Perov, V. (2005). Application of a New Spectral Theory of Stably Stratified Turbulence to the Atmospheric Boundary Layer over Sea Ice. *Boundary-Layer Meteorology*, 117(2), 231–257. doi: 10.1007/s10546-004-6848-4
- Svensson, G., & Holtslag, A. A. (2006). Single column modeling of the diurnal cycle based on CASES99 data-GABLS second intercomparison project. In *Preprints, 17th Symp. on Boundary Layers and Turbulence, San Diego, CA, Amer. Meteor. Soc., CD-ROM* (Vol. 8).
- Therry, G., & Lacarrère, P. (1983). Improving the Eddy Kinetic Energy model for planetary boundary layer description. *Boundary-Layer Meteorology*, 25(1), 63–88. doi: 10.1007/BF00122098
- Xie, B., & Fung, J. C. H. (2014). A comparison of momentum mixing models for the planetary boundary layer. *Journal of Geophysical Research: Atmospheres*, 119, 2079 – 2091.
- Xie, B., Fung, J. C. H., Chan, A., & Lau, A. (2012). Evaluation of nonlocal and local planetary boundary layer schemes in the WRF model. *Journal of Geophysical Research: Atmospheres*, 117(D12). doi: <https://doi.org/10.1029/2011JD017080>
- Xie, B., Hunt, J. C. R., Carruthers, D. J., Fung, J. C. H., & Barlow, J. F. (2013, July). Structure of the planetary boundary layer over Southeast England: Modeling and measurements. *Journal of Geophysical Research: Atmospheres*, 118(14), 7799–7818. doi: 10.1002/jgrd.50621
- Yan, B., Chan, P. W., Li, Q., He, Y., & Shu, Z. (2021). Dynamic analysis of meteorological time series in Hong Kong: A nonlinear perspective. *International Journal of Climatology*, 41(10), 4920–4932. doi: 10.1002/joc.7106
- Zhang, C., Wang, Q., Chan, P. W., Ren, C., & Li, Y. (2022). The effect of background wind on summertime daily maximum air temperature in Kowloon, Hong Kong. *Building and Environment*, 210, 108693. doi: <https://doi.org/10.1016/j.buildenv.2021.108693>
- Zhang, W., Fung, J. C. H., & Wong, M. F. M. (2023, August). *TKE-ACM2 planetary boundary layer scheme incorporated in WRF 4.3*. Zenodo. Retrieved from <https://doi.org/10.5281/zenodo.8275008> doi: 10.5281/zenodo.8275008
- Zonato, A., Martilli, A., Jimenez, P. A., Dudhia, J., Zardi, D., & Giovannini, L. (2022). A New K- $\epsilon$  Turbulence Parameterization for Mesoscale Meteorological Models. *Monthly Weather Review*, 150(8), 2157–2174. doi: 10.1175/MWR-D-21-0299.1